Journal of Magnetism and Magnetic Materials 417 (2016) 49–55

Contents lists available at ScienceDirect

Journal of Magnetism and Magnetic Materials

journal homepage: www.elsevier.com/locate/jmmm

# The influence of 1,2-alkanediol on the crystallinity of magnetite nanoparticles

Fernando B. Effenberger [a], A.W. Carbonari [b,*], L.M. Rossi [c]

[a] Centro Universitário da FEI, Av. Humberto de Alencar Castelo Branco, 3972, 09850-901 São Bernardo do Campo, Brazil
[b] Instituto de Pesquisas Energéticas e Nucleares, Universidade de São Paulo, 05508-000 São Paulo, SP, Brazil
[c] Instituto de Química, Universidade de São Paulo, Av. Prof. Lineu Prestes, 748, 05508-000 São Paulo, Brazil

ARTICLE INFO

*Article history:*
Received 26 February 2016
Received in revised form
29 April 2016
Accepted 10 May 2016
Available online 12 May 2016

*Keywords:*
$Fe_3O_4$
Nanoparticles
Magnetic hyperfine field

ABSTRACT

Magnetic nanoparticles of magnetite have been synthesized by thermal decomposition and investigated by measuring the magnetic hyperfine field. Preformed $Fe_3O_4$ nanoparticles were used as seeds to produce a series of magnetic nanoparticles, with different sizes and shapes. Samples were characterized by X-ray diffraction, transmission electron microscopy, and magnetization measurements. The perturbed angular correlation (PAC) technique was used to study the influence of 1,2-octanediol on the seeding growth of the $Fe_3O_4$ by measuring hyperfine interactions. The nuclear probes $^{111}In \rightarrow {}^{111}Cd$ were introduced into the samples through the synthesis of first core of $Fe_3O_4$, remained in the samples after the consecutive growth. The PAC results show the presence of two probe site fractions, one characterized by a well-defined magnetic dipole frequency with population $f_I$ and another characterized with a broad distributed electric quadrupole frequency with population $f_O$, which were, respectively, assigned to probes at substitutional Fe sites in crystalline $Fe_3O_4$ formed at inner region of the nanoparticles and probes at non-crystalline iron oxide in the outer region of nanoparticles. A mathematical model was proposed to fit the behavior of $f_O$ with the particle size.



## 1. Introduction

The magnetic properties of $Fe_3O_4$ nanoparticles are object of investigation in different areas where they are of fundamental importance to the development of several applications such as data recording, energy, catalysis, hyperthermia, drug delivery, magnetic separation, and magnetic resonance imaging [1–4]. Nanomaterials display novel physical and chemical properties which are different from those of bulk materials due to their small size. When the size of particles is reduced to the nanometer scale, surface effects become progressively more important and can, consequently, alter their magnetic properties, which can be attributed to an increase in the particle surface-area-to-volume ratio. This ratio reflects the increase in the amount of atoms at the surface and near surface region when compared to that in the nanoparticle core. When the shape of nanoparticles is changed, the relation between surface and core regions is changed too causing variations in the magnetic moment distribution, which affect the magnetic properties of particles [5].

In order to control size and shape (the synthesis of size controlled nanoparticles) a large number of physical and chemical routes have been developed, and thermal decomposition process stands out amid them with good control of the size of nanoparticles. Thermal decomposition (TD) is also considered as a versatile technique which allows the synthesis of particles with several shapes and can be used to synthesize metallic nanoparticles, metal alloys, oxides, core–shell structures, and seed growth [6–8].

In this paper, we have investigated, via hyperfine interactions, a series of magnetite nanoparticles prepared with two different seed growth in the presence and absence of 1,2-octanediol, which were characterized by perturbed gamma–gamma angular correlation (PAC) spectroscopy using $^{111}Cd$ as probe nuclei. The PAC spectroscopy is based on the observation of hyperfine interactions between nuclear moments of radioactive probe nuclei with extranuclear magnetic fields ($B_{hf}$) or an electric field gradient (efg). The PAC technique measures the time evolution of the $\gamma$-radiation emission pattern by the probe nuclei caused by the hyperfine interactions. PAC spectroscopy offers, therefore, a high degree of sensitivity to local structure variations in the crystal lattice and, as a consequence, can be used to follow crystal properties such as symmetry, defect trapping/de-trapping, magnetic spin distributions, magnetic moment formation, exchange interactions, etc. on an atomic scale and, thereby, sensing the chemical environment

* Corresponding author.
*E-mail address:* carbonar@ipen.br (A.W. Carbonari).

http://dx.doi.org/10.1016/j.jmmm.2016.05.028
0304-8853/

around the probe atoms. For materials with magnetic ordering, the measurement of hyperfine interactions, due to the short range of the interaction, is able to observe local fields, and consequently, if different phases are present in the material, it is also able to detect them yielding the fraction as well as the $B_{hf}$, efg or a combination of the magnetic hyperfine field plus electric field gradient of each one. Theoretical fundamentals as well as excellent reviews on PAC spectroscopy and their relevance to the study of condensed matter and materials sciences can be found in the literature [9–12].

## 2. Experimental procedure

### 2.1. Particle synthesis

The seeds of two different sets of magnetite nanoparticle samples (hereafter referred to as set A and set B) were synthesized by thermal decomposition following Sun's protocol [7]. In this synthesis, 2 mmol of Fe (III) acetylacetonate were dissolved in 6 mmol of oleic acid (OA), 4 mmol of oleylamine and 20 mL of diphenyl ether. The mixture was heated at 265 °C for 2 h under nitrogen flow and magnetic stirring. After the mixture was cooled down to room temperature, the nanoparticles were precipitated by adding ethanol and separated through centrifugation at 7000 rpm. This last process was repeated several times until the supernatant solution became clear.

The nanoparticle growth process for both set A and set B was performed as follows: 0.33 mmol $Fe_3O_4$ were dispersed in 6 mmol of OA, 4 mmol of oleylamine and 20 mL of diphenyl ether. This mixture was heated at 265 °C for 2 h under nitrogen flow and magnetic stirring. After the mixture was cooled down to room temperature, the nanoparticles were precipitated by adding ethanol and separated through centrifugation at 7000 rpm. This last process was repeated several times until the supernatant solution became clear.

For nanoparticles of set A, all synthesis was performed in the presence of 10 mmol of 1,2-octanediol and for set B all synthesis was performed in the absence of 1,2-octanediol. The size of particles was increased by repeating the growth process which was performed once, twice and thrice for each set producing samples of different sizes named A1, A2, and A3 for set A and B1, B2, and B3 for set B.

### 2.2. Particle characterization

Samples of set B had their structure analyzed by X-ray diffractometry (XRD) and the results, shown in Fig. 1, indicated that the samples have a single phase with the magnetite structure.

The morphology and size of all studied samples were investigated by transmission electron microscopy (TEM). All TEM images were obtained on a Philips CM 200 microscope operating at an accelerating voltage of 200 kV. The samples for TEM measurements were prepared by placing a drop of a toluene solution containing the nanoparticles in a carbon coated copper grid, followed by evaporation at room temperature under $N_2$ atmosphere. All samples had their magnetic properties characterized by magnetization measurements in a Lake Shore model 7407 vibrating sample magnetometer (VSM) at 5 K, 83 K and 300 K.

### 2.3. PAC spectroscopy measurements

A volume containing approximately 20 μCi of carrier-free $^{111}$In in the form of indium chloride solution was added to the sample solutions during the synthesis of the first seed of each set of samples. The $^{111}$In nucleus decays, by electron capture ($T_{1/2}$=2.7 days) to the excited states of $^{111}$Cd, which was used as

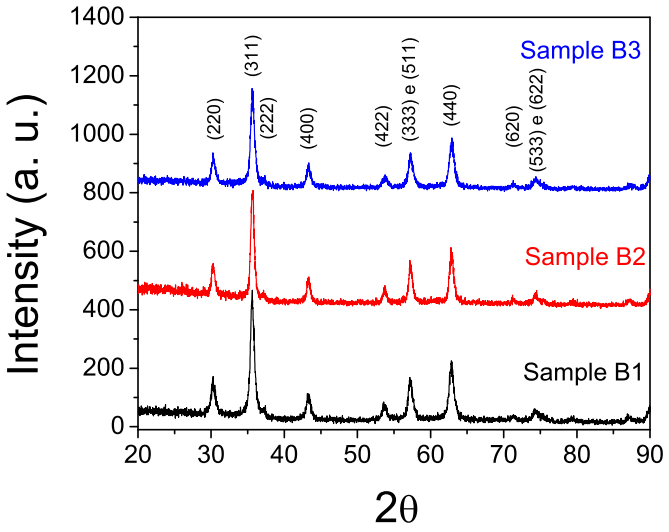


**Fig. 1.** XRD patterns for nanoparticles of set B: samples B1, B2, and B3, respectively, from bottom to top.

probe nucleus in the PAC measurements. The intermediate state with 245 keV and $5/2^+$ spin of the well known 171–245 keV $\gamma$–$\gamma$ cascade of $^{111}$Cd has been used to measure the hyperfine interactions. After centrifugation, the samples were measured at room temperature in the PAC spectrometer consisting of a standard setup with four $BaF_2$ detectors arranged in a planar 90–180° geometry, generating simultaneously 12 delayed coincidence spectra. The perturbation function obtained in a typical PAC experiment is given by

$$R(t) = 2\frac{C(180°, t) - C(90°, t)}{C(180°, t) + 2C(90°, t)}, \quad (1)$$

where $C(\theta, t)$ are the geometric mean of the background-subtracted coincidence spectra recorded at angle $\theta$. The measured perturbation function in samples is modeled by:

$$R(t) = A_{22}G_{22}(t) = A_{22}\sum_i f_i G^i_{22}(t), \quad (2)$$

where $A_{22}$ is the unperturbed angular correlation coefficient, $f_i$ are the fractional site populations, which takes into account the fact that the probe nuclei can occupy different sites into the samples, and $G^i_{22}(t)$ are the corresponding perturbation factors, which depends on the type of hyperfine interaction sensed by the probe nuclei, i.e., electric quadrupole, magnetic dipole or combined electric quadrupole plus magnetic dipole.

The perturbation factor $G_{22}(t)$ of the correlation function contains, therefore, detailed information about the hyperfine interaction between the probe nuclei and the local distribution of electronic charge and spins in their neighborhood. The experimental determination of $G_{22}(t)$ permits, for pure electric quadrupole interactions, the calculation of the spin-independent quadrupole frequency, defined by $\nu_Q = eQV_{zz}/h$, where $Q$ is the nuclear quadrupole moment of the intermediate nuclear level, and the asymmetric parameter $\eta = (V_{xx} - V_{yy})/V_{zz}$, where $V_{xx}$, $V_{yy}$ and $V_{zz}$ are the non-vanishing electric field gradient components in the principal-axis system with $|V_{xx}| \le |V_{xx}| \le |V_{xx}|$. For the pure dipole magnetic interaction, the Larmor frequency $\omega_L = g\mu_N B_{hf}/\mathrm{hbar}$ can be determined from $G_{22}(t)$, which allows the calculation of the magnetic hyperfine field $B_{hf}$ at the probe sites if the value of the $g$ factor of the intermediate level is known. Because $Fe_3O_4$ has cubic crystalline structure, electric quadrupole interactions are not expected at room temperature and, therefore, the perturbation factor for an unpolarized ferromagnetic sample consisting of randomly oriented domains with pure magnetic dipole interaction can be

written (neglecting the $A_{44}$ terms) as:

$$G_{22}(t) = [0.2 + 0.4\cos(\omega_L t) + 0.4\cos(2\omega_L t)], \quad (3)$$

Electric quadrupole interactions in $Fe_3O_4$ are expected if probe nuclei are embedded in an environment where the symmetry around them is non-cubic as a result of defects such as vacancies, structural or interstitial defects. The perturbation factor for electric quadrupole interactions is:

$$G_{22}(t) = S_{20} + \sum_{n=1}^{3} S_{2n}(\eta)\cos[g(\eta)\nu_Q t], \quad (4)$$

where $g(\eta)$ coefficients describe the electric quadrupole splitting of the intermediate state of the probe nuclei and $S_{2n}$ are coefficients of the transition frequencies between the sublevels from the split of the intermediate state.

Effects of finite time resolution ($\tau_R$) of detectors and the distribution of frequencies ($\delta$) are properly taken into account in the perturbation factor by the function $G(\tau_R, \delta) = \exp(-fq^2\tau_R^2/2)\exp(-fq^2\delta^2t^2/2)$, with $fq$ being $\omega_L$ or $\nu_Q$, for dipole magnetic or electric quadrupole interactions, respectively. Details regarding PAC experimental methodology can be found elsewhere [13,14].

## 3. Results

Figs. 2 and 3 display gray-scale TEM images along with particle

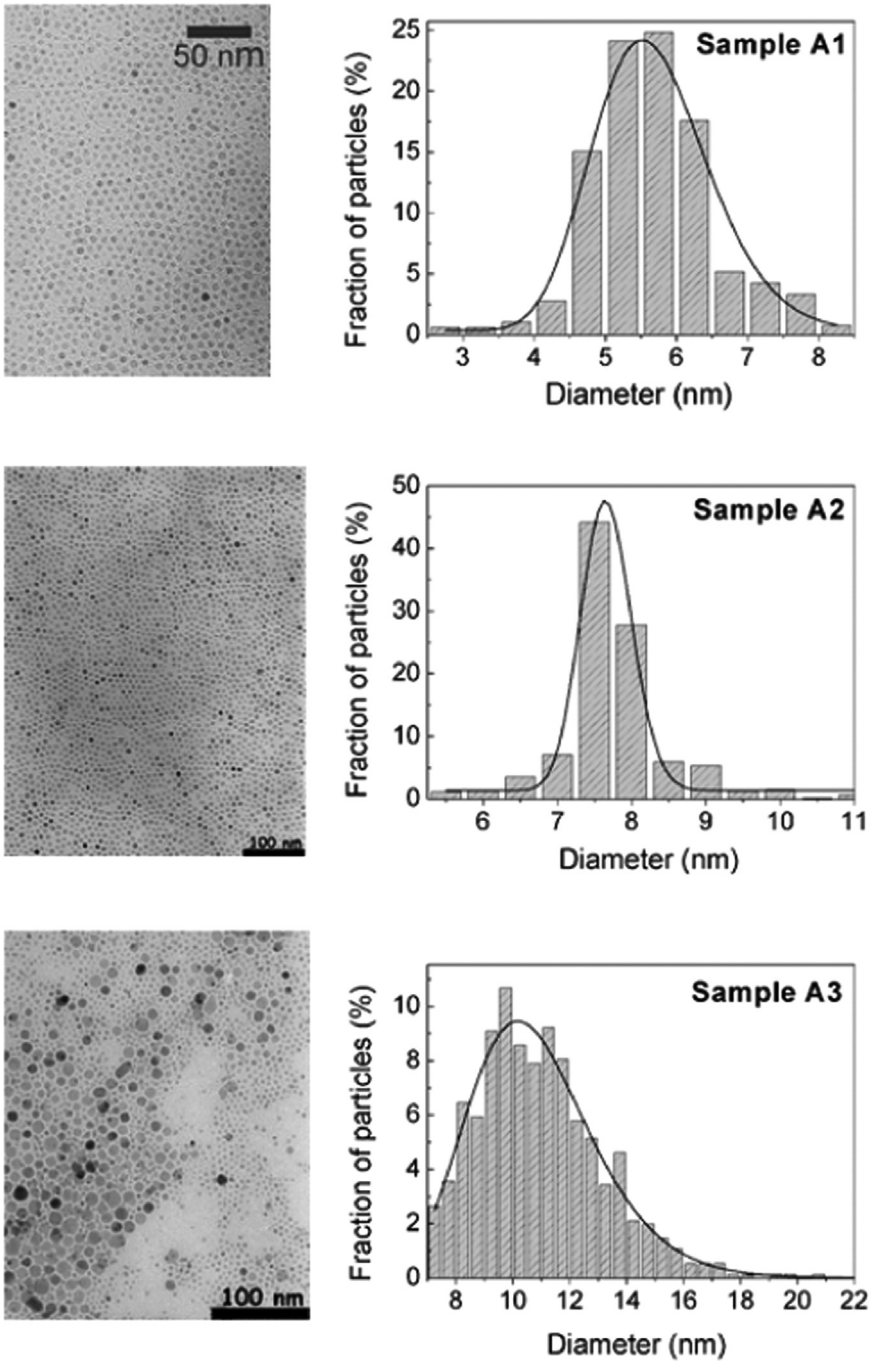


**Fig. 2.** TEM images for samples A1, A2, and A3 of set A (left) and the corresponding histogram (right) fitted with a log-normal distribution to estimate the mean particle size. Solid lines are the log-normal curve.

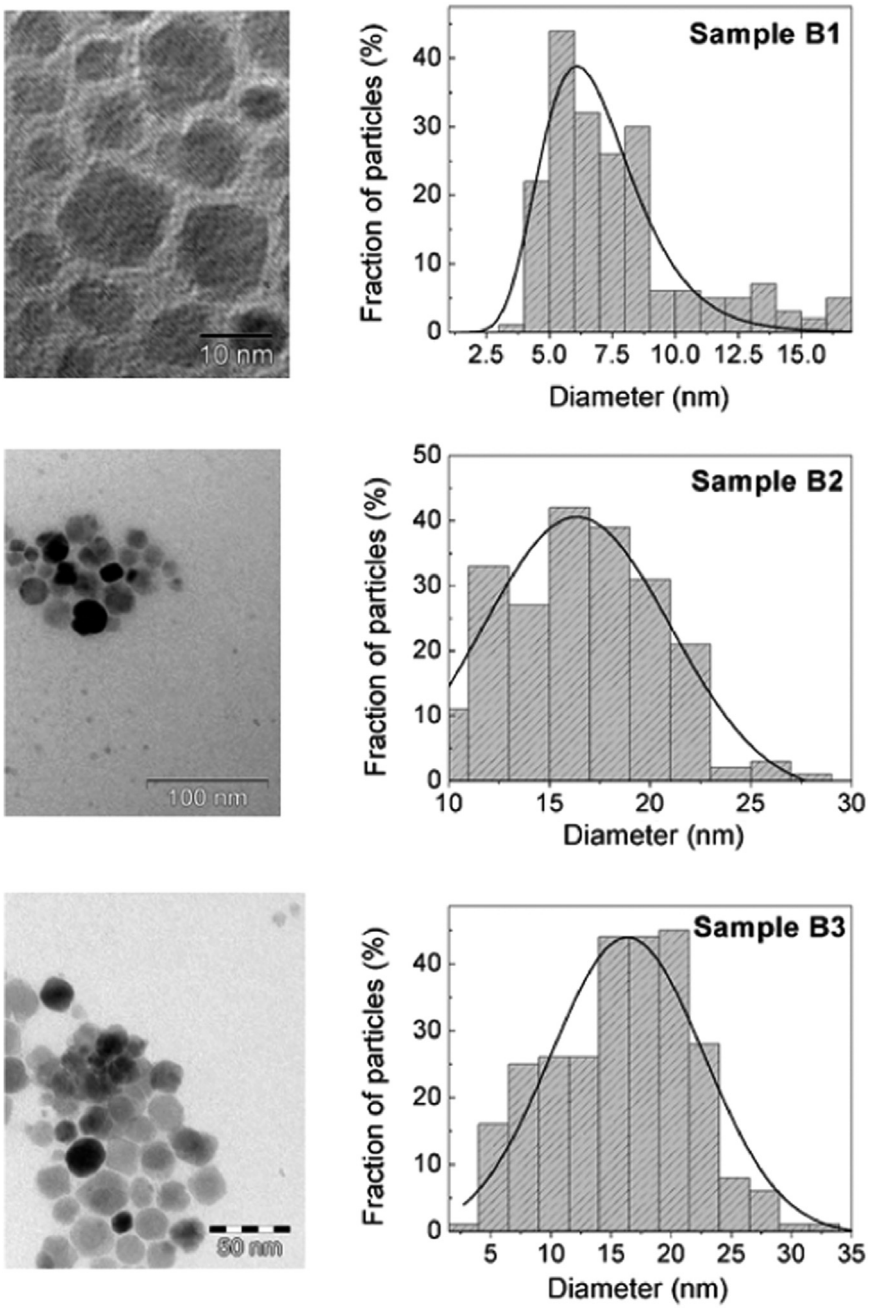


**Fig. 3.** TEM images for samples B1, B2, and B3 of set B (left) and the corresponding histogram (right) fitted with a log-normal distribution to estimate the mean particle size. Solid lines are the log-normal curve.

size distribution histograms for samples of set A and set B, respectively. As can be easily seen, samples of set A have spherical-like shape nanoparticles and samples of set B have cubic-like shape nanoparticles. Results for the average diameter of nanoparticles of each group are displayed in Table 1.

We have performed the TD synthesis in the presence 1,2-octanediol for samples of set A and the results show well dispersed spherical-like shaped nanoparticles of 5.6 nm of average size for particle of sample A1 with narrow size distribution ($\sigma = 0.12$) (see Fig. 2). It is interesting to notice that the absence of the 1,2-octanediol in the TD synthesis, performed under similar conditions, resulted in the growth of cubic-like shaped NPs with average size of ~6.6 nm for sample B1. Moreover, the absence of the 1,2-octanediol produced samples with larger average size than those synthesized with the 1,2-octanediol under the same conditions, as displayed in Table 1. This behavior suggests a definite influence of the 1,2-alkanediol on the TD process, contributing to the improvement of the NPs dispersion, size, and size distribution. It is somewhat difficult to determine precisely how this molecule is affecting the nucleation or crystal growth process but studies are

**Table 1**
TEM results for the average (av.) size of studied nanoparticles.

| Set A | | Set B | |
|---|---|---|---|
| Sample | Av. size (nm) | Sample | Av. size (nm) |
| A1 | 5.6 | B1 | 6.6 |
| A2 | 7.4 | B2 | 16.5 |
| A3 | 10.6 | B3 | 17.3 |

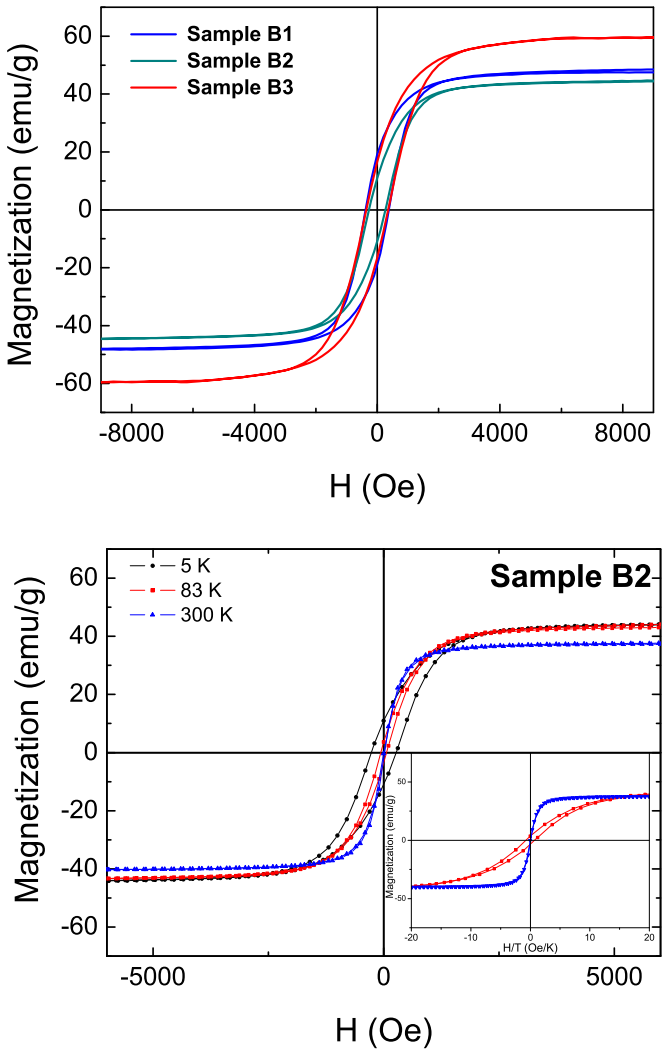


**Fig. 4.** Magnetization as a function of the applied field for samples of set B measured at 5 K (top) and magnetization versus applied field for sample B3 at three different temperatures (bottom). The inset in the bottom shows the magnetization curves at 300 K and 83 K as a function of $H/T$.

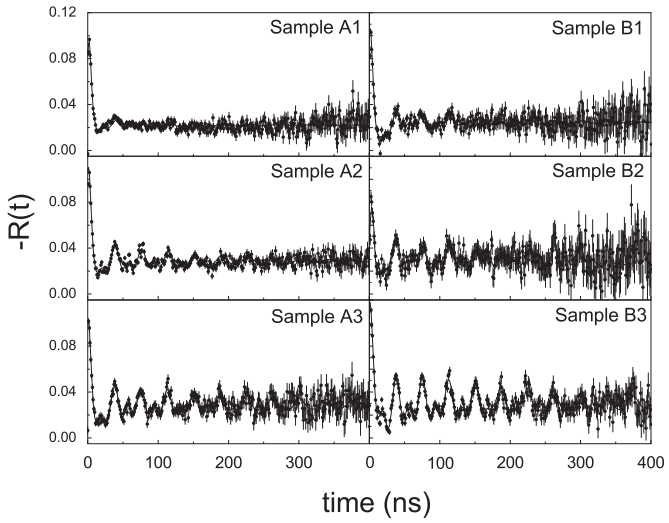


**Fig. 5.** Perturbation functions for $^{111}$Cd probes in $Fe_3O_4$ for set A (left) and set B (right) samples displaying results for A1, A2, A3 and B1, B2, B3 samples, respectively. Solid lines are the least-squares fits of the theoretical function to the experimental data.

underway in order to clarify this point.

The transition from blocked to superparamagnetic state was characterized by measuring hysteresis of magnetization curves as a function of the applied field intensity at different temperatures. Magnetization measurement results showed that the coercivity ($H_c$) decreases when temperature increases, as expected (see Fig. 4). The temperature dependence of the coercivity for non-interacting single-domain particles is given by

$$H_c(T) = H_c(0)[1 - aT^{1/2}], \tag{5}$$

where $H_c(0)$ is the coercivity at $T=0$, and $a = 25k_B/\mathrm{KV}$, with $K$ being the anisotropy constant, $k_B$ the Boltzmann constant, and $V$ the volume of the particle. From the results of magnetization measurements at different temperatures were possible to estimate the blocking temperature using Eq. (5). It was found that $T_B$ values are 108 K, 125 K, and 132 K, respectively for B1, B2 and B3 samples.

Some PAC spectra measured for the two sets of samples are displayed in Fig. 5. The first set of samples (left side in Fig. 5) crystallizes in spherical-like shape while the second set of samples (right side in Fig. 5) crystallizes in cubic-like shape as can be seen in TEM images. A visual inspection of the spectra shows that the amplitude of the peaks, which indicates a well-defined magnetic hyperfine frequency, increases as the diameter of the nanoparticle increases.

All spectra were measured at room temperature and show a strong magnetic dipole interaction which should not be present if the system is above the blocking temperature where a paramagnetic behavior takes place. This observation occurs because superparamagnetism is not only implicitly dependent on temperature, but also on the measurement time window ($\tau_M$) of the experimental technique used to measure it, when compared to the relaxation time ($\tau$) for the reversal of the magnetic moment of single-domain particles. This thermally activated process is governed by the rate of flipping over an energy barrier $\Delta E = KV$ (where $K$ is the magnetic anisotropy energy density and $V$ is the particle volume) and is described by

$$\tau = \tau_0 \exp(\Delta E/k_B T), \tag{6}$$

where $\tau_0$ is the pre-exponential factor, which, for non-interacting particles, is of the order $10^{-9}$–$10^{-13}$ s. At temperatures $T > T_B$, if the measurement time window $\tau_M \gg \tau$, the flipping is fast relative to the experimental time window and the particles appear to be paramagnetic, because this fast relaxation makes the magnetic interactions to be averaged to zero. Conversely, if $\tau_M \ll \tau$, the flipping is slow and quasi-static magnetic properties are observed, the system is consequently in a blocked state. For PAC spectroscopy as well as Mössbauer spectroscopy, the measurement time window is typically in the range of $10^{-8}$–$10^{-9}$ s, which is much smaller than that for magnetization measurements ($\tau_M \sim 10^2$ s). Consequently, using Eq. (6), the calculated ration between the blocking temperatures from PAC spectroscopy ($T_B^{PAC}$) and magnetization measurements ($T_B^{MAG}$) is $T_B^{PAC}/T_B^{MAG} \approx 7$. Experimentally, the ratio for Mössbauer spectroscopy and magnetization measurements was found to be ~3–5 [15,16]. As the blocking temperatures for samples of group 2 measured with magnetization are in the range 108–132 K, at room temperature, PAC will observe the systems in the blocked state and, consequently, the dipole magnetic hyperfine interaction given by Eq. (3) is present.

## 4. Discussion

A model for theoretical perturbation function consisting of two probe sites (hereafter referred to as site I and site O) was least-

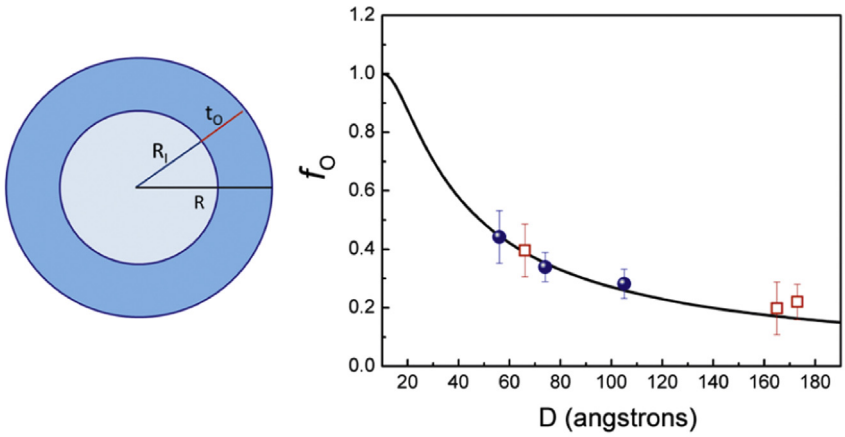


**Fig. 6.** Schematic drawing of two regions inside the NP (left). Fraction of the outer shell as a function of the size of the NP (right). The full circles are data for spherical NP and the open squares are data for cubic NP. The solid line represents the fit of expression given by Eq. (9) (see text).

square fitted to experimental PAC data. Results of the fit yield a well-defined magnetic frequency $\omega_L{}^I$ ~168 Mrad/s to site I and a widely distributed ($\delta$ ~50%) electric quadrupole frequency $\nu_Q{}^O$ in the range of 120–160 MHz to site O. The frequency $\omega_L{}^I$ is equal to that measured with $^{111}$Cd at Fe sites in $Fe_3O_4$ [17]. We have, therefore, assigned $\omega_L{}^I$ to the magnetic dipole interaction of $^{111}$Cd nuclei at Fe sites in crystalline $Fe_3O_4$ formed at inner region of the nanoparticle. The second widely distributed frequency $\nu_Q{}^O$ was assigned to $^{111}$Cd probes at non-crystalline iron oxide in the outer region of nanoparticle, near the surface where defects are present, plus probe nuclei embedded in the coated material at the region outside the nanoparticle. Fig. 6 (right) shows a schematic drawing of these two regions in the nanoparticle. It was observed that the fraction corresponding to the outer region ($f_O$) decreases as the size of the particles increases as it is shown in Fig. 6 (left) for PAC results from measurements of set A (spherical particles) and set B (cubic particles) of samples.

Considering that the probe nuclei are homogeneously distributed for the entire nanoparticle samples, and also taken into consideration that the particles have two regions, the inner core and the outer shell, as shown in Fig. 6, it is possible to calculate the fraction of probe nuclei in both regions. The fraction of probe nuclei in each region is therefore directly proportional to the relative volume of the region with respect to the volume of the nanoparticle. For spherical particles, the fraction of probe nuclei in the outer shell of the nanoparticle is thus proportional to

$$f_O \propto 1 - \left(\frac{R - t_O}{R}\right)^3, \tag{7}$$

where $R$ is the radius and $t_O$ is the thickness of the outer shell of the nanoparticle. The thickness $t_0$ is reasonable to be considered slightly greater than the lattice parameter of $Fe_3O_4$, which is $a$=8.3967 Å [18]. In our calculations we, therefore, considered $t_O$ =10 Å for all particle sizes.

However, part of probe nuclei can lie in the coating material outside the particles and also present a highly distributed PAC frequency. It is reasonable to consider that the probability of the probe nuclei be in this region is the same for nanoparticles of all sizes and, as a consequence, the contribution of these nuclei to the widely distributed fraction is constant and does not affect the behavior of the fraction $f_O$ with the size of the particles. In order to take into account this contribution and estimate the fraction $f_O$, we have normalized the value for the sample with 5.6 nm to the calculated value and subtracted the difference from all other values. The normalized values are shown in Fig. 6 as full circles. The fraction $f_O$ for samples from set B, normalized by the same factor of samples in set A, are also shown in the figure as open squares. It was then observed that the results for cubic nanoparticles follow the same behavior of that for spherical nanoparticles.

If we consider that cubic nanoparticles also have two regions, the inner well crystallized region and the outer region where the presence of defects strongly affect the way the atoms are arranged, it is also possible to calculate the fraction $f_O$, which in this case is given by:

$$f_O \propto 1 - \left(\frac{l - 2t_O}{l}\right)^3, \tag{8}$$

where $l$ is the side length of the cubic nanoparticle and $t_O$ is the thickness of the outer shell of the nanoparticle. So as to compare the two equations it is reasonable to express Eq. (7) in terms of the total extension of the nanoparticle as it is in Eq. (8). Re-writing Eq. (7) this time using the diameter $D$ of the nanoparticle instead of the radius, we obtain:

$$f_O \propto 1 - \left(\frac{D - 2t_O}{D}\right)^3, \tag{9}$$

Eqs. (8) and (9), which calculate the fraction of probe nuclei at the outer region of cubic and spherical nanoparticles, respectively, indicate the $f_O$ has the same behavior in both cases, as it was experimentally observed and displayed in Fig. 6, where the result for the calculated fraction $f_O$ is also shown as a solid line. We, therefore, can conclude that the shape of the nanoparticle does not have influence on the crystallization of the particles and Eqs. (8) and (9) can be useful to predict the crystallization of the particles from its total extension.

## 5. Conclusion

Nanoparticles of $Fe_3O_4$ were synthesized by the thermal decomposition method with and without the presence 1,2-octanediol. Results of characterization measurements show that the resulting particles are well dispersed with narrow size distribution and have spherical-like shape but those synthesized with 1,2-octanediol present a cubic-like shape. Results also show that the absence of the 1,2-octanediol produced samples with larger average size than those synthesized with the 1,2-octanediol under the same conditions. Magnetization measurements showed a superparamagnetic behavior above blocking temperatures in the range

from ~110 K to ~130 K, depending on the size of particles. We use a nuclear technique, the PAC spectroscopy, capable of distinguishing different regions inside samples, to characterizing the nanoparticles, measuring the hyperfine interactions and the population of site fractions corresponding to probes in the inner part of particles, which is crystalline and presents a $B_{hf}$ with the known value for bulk $Fe_3O_4$, and in the outer part, which is non-crystalline. With the results of fraction population as a function of particle size it was possible to formulate a model to calculate the fraction population of probe nuclei at the outer region of both cubic and spherical nanoparticles. The results show the same behavior of the fraction population for both cases. We then conclude that the shape of the nanoparticle does not have influence on their crystallization. The proposed model is, therefore, useful to predict the crystallization of the particles from their size.

## Acknowledgments

Partial support for this research was provided by the Fundação de Amparo à Pesquisa do Estado de São Paulo (FAPESP) grant no. 2012/11104–9. A.W.C. thankfully acknowledges the support provided by CNPq (grant no. 305046/2013–6) in the form of research fellowships.

## References

[1] Q.A. Pankhurst, J. Connolly, S.K. Jones, J. Dobson, J. Phys. D 36 (2003) R167.
[2] U. Jeong, X. Teng, Y. Wang, H. Yang, Y. Xia, Adv. Mater. 19 (2007) 33.
[3] N. Tran, T.J. Webster, J. Mater. Chem. 20 (2010) 8760.
[4] Shih-Hung Huang, Ruey-Shin Juang, J. Nanopart. Res. 13 (2011) 4411.
[5] A.H. Morrish, The Physical Principles of Magnetism, John Wiley & Sons, Hoboken, NJ 2001, p. 332.
[6] T. Hyeon, S.S. Lee, J. Park, Y. Chung, H.B. Na, J. Am. Chem. Soc. 123 (2001) 12798.
[7] S. Sun, H. Zeng, J. Am. Chem. Soc. 124 (2002) 8204.
[8] A.H. Latham, M.E. Williams, Acc. Chem. Res. 41 (2008) 411.
[9] R.M. Steffen, H. Frauenfelder, The influence of extranuclear fields on angular correlation, in: E. Karlsson, E. Matthias, K. Siegbhan (Eds.), Perturbed Angular Correlations, North-Holland Publishing Co, Amsterdam, 1964, p. 1.
[10] M. Uhrmacher, Defect Diffus. Forum 311 (2011) 105.
[11] A.W. Carbonari, J. Mestnik-Filho, R.N. Saxena, Defect Diffus. Forum 311 (2011) 39.
[12] G. Schatz, A. Weidinger, Nuclear Condensed Matter Physics: Nuclear Methods and Applications, John Wiley & Sons, Chichester, England 1996, p. 63.
[13] R. Dogra, A.C. Junqueira, R.N. Saxena, A.W. Carbonari, J. Mestnik-Filho, M. Morales, Phys. Rev. B 63 (2001) 224104.
[14] A.W. Carbonari, R.N. Saxena, W. Pendl Jr., J. Mestnik-Filho, R.N. Atilli, M. Olzon-Dionysio, S.D. de Souza, J. Magn. Magn. Mater. 163 (1996) 313.
[15] B.H. Sohn, R.E. Cohen, G.C. Papaefthymiou, J. Magn. Magn. Mater. 182 (1996) 216.
[16] E. Lima Jr., A.L. Brandl, A.D. Arelaro, G.F. Goya, J. Appl. Phys. 99 (2006) 083908.
[17] Z. Inglot, D. Wiarda, K.P. Lieb, T. Wenzel, M. Uhrmacher, J. Phys.: Condens. Matter 3 (1991) 4569.
[18] S. Weissmann, B. Post, M.E. Mrose, H.F. McMurdie, M.C. Morris, W.F. McClune, Selected Powder Diffraction Data for Metals and Alloys, 1st edition, JCPDS International Centre for Diffraction Data: Swarthmore, 1978.